



Aerosols in Healthy and Emphysematous In Silico Pulmonary Acinar Rat Models

Jessica M. Oakes, Philipp Hofemeier, Irene Vignon-Clementel, Josué Sznitman

► To cite this version:

Jessica M. Oakes, Philipp Hofemeier, Irene Vignon-Clementel, Josué Sznitman. Aerosols in Healthy and Emphysematous In Silico Pulmonary Acinar Rat Models. *Journal of Biomechanics*, 2016, 49 (11), pp.2213-2220. 10.1016/j.jbiomech.2015.11.026 . hal-01244458

HAL Id: hal-01244458

<https://inria.hal.science/hal-01244458>

Submitted on 15 Dec 2015

HAL is a multi-disciplinary open access archive for the deposit and dissemination of scientific research documents, whether they are published or not. The documents may come from teaching and research institutions in France or abroad, or from public or private research centers.

L'archive ouverte pluridisciplinaire **HAL**, est destinée au dépôt et à la diffusion de documents scientifiques de niveau recherche, publiés ou non, émanant des établissements d'enseignement et de recherche français ou étrangers, des laboratoires publics ou privés.

6 Abstract

7 There has been relatively little attention given on predicting particle deposition in the respi-
8 ratory zone of the diseased lungs despite the high prevalence of chronic obstructive pulmonary
9 disease (COPD). Increased alveolar volume and deterioration of alveolar septum, characteristic of
10 emphysema, may alter the amount and location of particle deposition compared to healthy lungs,
11 which is particularly important for toxic or therapeutic aerosols. In an attempt to shed new light on
12 aerosol transport and deposition in emphysematous lungs, we performed numerical simulations in
13 models of healthy and emphysematous acini motivated by recent experimental lobar-level data in
14 rats [17]. Compared to healthy acinar structures, models of emphysematous subacini were created
15 by removing inter-septal alveolar walls and enhancing the alveolar volume in either a homogeneous
16 or heterogeneous fashion. Flow waveforms and particle properties were implemented to match the
17 experimental data. The occurrence of flow separation and recirculation within alveolar cavities was
18 found in proximal generations of the healthy zones, in contrast to the radial-like airflows observed
19 in the diseased regions. In agreement with experimental data, simulations point to particle depo-
20 sition concentrations that are more heterogeneously distributed in the diseased models compared
21 with the healthy one. Yet, simulations predicted less deposition in the emphysematous models in
22 contrast to some experimental studies, a likely consequence due to the shallower penetration depths
23 and modified flow topologies in disease compared to health. These spatial-temporal particle trans-
24 port simulations provide new insight on deposition in the emphysematous acini and shed light on
25 experimental observations.

26 Introduction

27 While computational models that describe the behaviour of inhaled particles in the respiratory
28 acinar regions of the healthy lung have attracted broad attention [8, 10, 13–15], little focus has
29 yet been made on modelling the transport of aerosols in the diseased pulmonary acinus. To the

best of our knowledge, no 3D *in silico* acinar models have attempted to address the fate of inhaled micron-sized aerosols in the context of pulmonary conditions such as emphysema. Emphysema is a progressively severe heterogeneous obstructive disease caused by inhalation of toxic gases and particles over a long period of time [11]. The disease is characterized by alveolar airspace enlargement caused by deterioration of the pulmonary tissue leading to a loss of interalveolar septa [30]. At its earliest stages the diseased lesions are heterogeneously distributed in the lung; however, as the disease progresses inflammation, protease activity, and remodelling leads to a more severe and widespread distribution of damaged tissue [24, 25]. Due to the increased resistance of the small airways and tissue compliance, the lung takes a longer time to empty [11], which may lead to ventilation asymmetry [19], air trapping [12], and ventilation deficiency [4]. As aerosol medications are increasingly used to either treat pulmonary or systemic diseases, it is imperative to understand deposition in both healthy and diseased lungs. While effective treatment of emphysema is still unavailable, recent animal studies have suggested that biphosphonate (alendronate) inhalation, commonly used to treat osteoporosis, may have therapeutic potential by blunting the inflammatory response of alveolar macrophages [31].

Previous *in vivo* [3, 17, 26] and *in vitro* studies [1, 18] have attempted to uncover the behaviour of inhaled particles in the emphysematous lung. However, likely due to the progressive nature of the disease, there remains a lack of agreement on whether there are more or less particles depositing in the emphysematous lung compared to a healthy one. For example, Oakes et al. [17] found enhanced deposition in elastase-treated rat lungs compared to healthy ones measured with Magnetic Resonance Imaging (MRI), in contrast to earlier measurements obtained in elastase-treated hamsters where a decreased deposition was measured [26]. Yet, both animal studies [17, 26] agreed on the enhanced heterogeneity in the distribution of aerosol deposition patterns in the diseased lungs. In a 3D scaled-up *in vitro* studies, Oakes et al. [18] and Berg et al. [1] determined a decrease in penetration depth in an emphysematous alveolar sac and acinar model compared to healthy ones and

55 hypothesized that this would result in a decrease in deposition in the diseased models. This finding
56 agrees with decreased deposition in emphysema, compared to healthy lungs, found in a stochastic
57 model of various types of emphysema [23].

58 The advantage of numerically modelling the lung lies in the ability to investigate particle trans-
59 port and deposition at temporal and spatial resolutions that are currently beyond reach with current
60 state-of-the-art imaging modalities. Motivated by such shortcomings and available aerosol deposi-
61 tion data in rats [17], a computational framework has been recently developed to model airflow and
62 particle transport in anatomically-reconstructed conducting airways of rats [20]. While deposition
63 predictions between *in vivo* and *in silico* agreed well in healthy rats, similar agreement was not
64 found for the emphysematous animals [19]. As this *in silico* model did not include the small air-
65 ways and acinar region of the lung, the behaviour of particles once they reach the distal regions of
66 the lung remains widely unknown. It is hypothesized that the enlarged airspaces and deterioration
67 of the alveolar septa, characteristic of emphysema, will lead to noticeable differences in total and
68 spatial distribution patterns of particles.

69 The main aims of this study were to numerically investigate the deposition patterns in healthy
70 and diseased acini and to shed light on the transport mechanisms behind the enhanced deposi-
71 tion in emphysema found experimentally [19]. For such purpose, we adapted a numerical acinar
72 framework recently developed [10] and compared deposition predictions between a healthy rat
73 acinar model and two emphysematous cases. The emphysema models were created by enlarging
74 airspaces and removing connecting alveolar septa in either a homogeneous or heterogeneous fash-
75 ion. To facilitate comparison between our predictions and experimental data, both the ventilation
76 (i.e. breathing patterns) and particle properties were chosen to match the conditions implemented in
77 Oakes et al. [17]. By assessing the differences between healthy and diseased acini, our efforts aim
78 to advance the knowledge of inhaled particles in the deep regions of the diseased lung and pinpoint
79 the mechanisms responsible for the deposition differences between the healthy and emphysematous

80 rats.

81 **Methods**

82 *Rat Acinar Geometry*

83 Three distinct multi-generational rat acinar domains were designed following a space-filling
84 model of 3D polyhedral units [7, 27]. A healthy (H), heterogeneous emphysematous (E_{Het}) and
85 homogeneous emphysematous (E_{Hom}) models were created (Fig. 1a-c), where each acinar network
86 consists of up to six airway generations with a maximum of 277 polyhedral alveoli (Table 1). The
87 resulting sub-acini capture sufficiently well realistic full acinar structures [13]. A healthy human
88 acinar model [10] was scaled down by 15 % to match dimensions of a rat acinus [21] at functional
89 residual capacity (FRC) since interspecies differences are overall minor (see limitations below for
90 further discussion). The outer airway sleeve diameter, including the ducts and surrounding alveoli,
91 was held constant at $86\ \mu\text{m}$ with a characteristic alveolar diameter of $35\ \mu\text{m}$. Airway ducts spanned
92 a length of 56 to $85\ \mu\text{m}$, depending on generation.

93 In order to capture and integrate some of the emphysema-like morphological changes, the H
94 model was modified according to two characteristics features: (i) removing the inter-alveolar septal
95 walls as highlighted in Fig. 1c (inset) and (ii) increasing the acinar volume of the model by adding
96 additional polyhedral structures in the bifurcation regions (see Table 1). Thus, diseased regions
97 were characterized as enlarged continuous airspaces without distinct alveolar cavities, in contrast
98 to the normal regions (compare Fig. 1a to d). The entire E_{hom} model was defined as diseased
99 and thus the emphysema-like changes were distributed throughout the model (see Fig. 1d and
100 Table 1). The E_{het} model represents a non-uniform distribution of emphysema where two zones
101 were created; a normal zone (N) and a diseased zone (D). The bottom right portion of the model
102 was prescribed as diseased as highlighted in grey in Fig. 1b leaving the rest of the model as normal
103 (Fig. 1c). FRC values for each model, including the two regions of the E_{het} model, are presented
104 in Table 1, showing that FRC increases with emphysema severity. In order to underline the loss of

septal walls, the number of alveolar cavities as well as the surface-to-volume ratio S/V are shown in Table 1; here, we find that S/V is approximately decreased by half for the E_{hom} model compared to the healthy condition. Corresponding videos presenting the acinar models and their respective breathing motions are supplied in the Supplementary Material (SM).

Respiration Curves

A self-similar breathing motion was prescribed across the entire acinar domain to simulate cyclic expansion and contraction motion following previous works [9, 10, 27]. Realistic respiration curves, derived from rat ventilation studies [17, 20], were scaled for each of the acinar models in order to match realistic tidal volumes. Specifically, the time-dependent acinar volumes were defined as $V_{H,A}(t) = \alpha V_{H,T}(t)$ and $V_{E,A}(t) = \alpha V_{E,T}(t)$ for the H and E_{hom} models, respectively; note that the indices A and T indicate acinar and total lung, respectively. Assuming that the acinar volume fraction of the H and E_{hom} models are identical, α was set to $FRC_{H,A}/FRC_{H,T}$, with $FRC_{H,T} = 4.77$ mL [22].

It is important to note that a straightforward scaling of the time-dependent volume curve is not feasible for the E_{het} model as the tissue mechanics of the normal and diseased zones are different. Following a recent approach [19], we scaled the curves separately for each region based on a lumped model where respiratory resistance (R) and compliance (C) are in series. Assuming that the normal region of the lung correlates with the healthy rat lung, R_N and C_N were set to $R_N = R_{H,T}/\alpha_N$ and $C_N = C_{H,T} * \alpha_N$, where $R_{H,T} = 0.098$ cm H₂O-s-cm⁻³ and $C_{H,T} = 0.236$ cm³ (cm H₂O)⁻¹. Here, $\alpha_N = \alpha FRC_{N,A}/FRC_{H,A}$ [19]. The respiratory volume curve of the normal region ($V_{N,A}(t)$) was found by directly solving

$$R_N \frac{dV_{N,A}(t)}{dt} + \frac{V_{N,A}(t)}{C_N} = P(t) - P_{peep}, \quad (1)$$

where $P(t)$ is the pressure measured at the trachea of the emphysematous rat during ventilation and P_{peep} is the positive expiratory pressure of 1 cm H₂O [19]. The respiratory volume curve of the

120 diseased region ($V_{D,A}(t)$) was calculated as $V_{D,A}(t) = TV_{D,A}^{V_{E,T}(t)}/TV_{E,T}$, where the tidal volume of
 121 the diseased region is defined as $TV_{D,A} = TV_{E,A} - TV_{N,A}$. The corresponding $V_{N,A}$ and $V_{D,A}$ were
 122 prescribed to the normal and diseased regions of the E_{het} model in the 3D flow simulations.

123 The resulting volume curves (i.e. $V_A(t)$ normalized by FRC_A) and flow rates over the cycles
 124 are shown for each acinar model in Fig. 2a and b, respectively. Note that the tidal volumes were
 125 the same for each model and were slightly larger in the diseased region compared to the normal
 126 region of the E_{het} model (Table 1 and Fig. 2). As shown in Oakes et al. [19], the decay rates of
 127 $V_{E,A}$ and $V_{D,A}$ were slower compared to the corresponding healthy curves (Fig. 2a). This resulted
 128 in lower peak flow rates during exhalation (Fig. 2b). Flow rates during inspiration were nearly the
 129 same for the H and E_{hom} models because all the rats were ventilated with identical settings [20].
 130 The diseased zone of E_{het} finished filling slightly after the corresponding normal zone, due to the
 131 longer time constant of the diseased region as shown in the inset of Fig. 2b, namely $\mathcal{T} = RC$ such
 132 that $\mathcal{T}_{N,A} = 0.023$ s and $\mathcal{T}_{D,A} = 0.045$ s.

133 *Flow and Particle Simulations*

134 Airflow and particle transport simulations were performed in OpenFOAM (Open Source Field
 135 Operation and Manipulation, Version 2.1.1). Airflow was modeled as a continuum using the
 136 finite volume method (FVM), where the Navier-Stokes equations were solved on an arbitrary
 137 Lagrangian-Eulerian (ALE) framework assuming air to be incompressible, Newtonian and at con-
 138 stant temperature (37°C). Further details on the numerical solver and discretization models has
 139 been recently discussed [10]. Briefly, airflow motion was induced by the expansion (inhalation)
 140 and contraction (exhalation) of the domain as described in the section above. At the inlet/outlet a
 141 constant pressure was imposed, since the flow field is generated as a result of the prescribed domain
 142 motion; note that the absolute pressure is not needed to solve the transport equation. Following pre-
 143 vious convergence studies, a total of 1.4M tetrahedral cells (H model) was used to discretize the
 144 acinar domain [10], where a total of four different mesh sizes were analyzed ranging from 0.7M to

145 5M cells. Here, a final mesh size of 1.4M tetrahedral cells was found to faithfully capture velocities
146 in the H model, which is anticipated to experience the highest velocity gradients compared to the
147 two other models. A dynamic time stepping was used to maintain the Courant-Friedrichs-Lewy
148 condition ($CFL < 1$) to capture rapid changes in the flow (i.e. velocity gradients) during exha-
149 lation [10]. The developed numerical algorithm was compared and validated with experimental
150 measurements [5] as well as analytical solutions [9, 10].

151 Neglecting electrostatic and hygroscopic effects, it is widely acknowledged that the main forces
152 acting on airborne spherical and inert particles at the micron scale are viscous drag (convection),
153 gravitational sedimentation, and Brownian diffusion [28]. Using Lagrangian particle tracking
154 methods, aerosol kinematics were solved from the particle momentum equation accounting for
155 drag, gravity and stochastic diffusion [10], where a one-way fluid particle coupling was used since
156 low particle concentrations are anticipated in the most distal acinar generations [10]. Particles were
157 injected by seeding particles (diameter = $1\mu m$, density = $1g/cm^3$) according to [17] continuously
158 over the first inspiration as a function of the local (and unsteady) velocity, thus mimicking a con-
159 stant concentration of injected particles. A total of 170,000 particles were injected and tracked over
160 two breathing cycles. Only $\sim 1\%$ of the injected particles remained airborne in the model after the
161 second breathing cycle.

162 **Results**

163 To assess the nature of acinar flow structures under emphysematous conditions, flow stream-
164 lines for the E_{het} model are shown in Fig. 3 at peak inspiration ($t = \tau/8$), where flow patterns for the
165 healthy and diseased regions are simultaneously compared. Flow topologies in ducts and alveoli
166 of healthy acini show characteristic configurations that evolve as a function of acinar generation
167 depth. Indeed, in proximal generations alveolar flows separate as a result of relatively high-shear
168 flows in the duct compared to slow, recirculating flows in the alveolar cavity (Fig. 3, top left).
169 As acknowledged to exist in distal acinar generations [6, 28], streamlines within alveolar cavities

170 feature radial-like structures, thus following more closely the motion of the alveolar walls in the
 171 absence of strong ductal flows (Fig. 3, top right). Alveolar flow patterns transition to half-open
 172 streamlines in medial generations (Fig. 3, bottom left), underlining the coupling between ductal
 173 shear flows and alveolar wall motion. In contrast to healthy regions, due to the absence of septa
 174 walls, flow patterns in the diseased regions lack the characteristic separation between ductal and
 175 alveolar flow regims. Instead, slow, quasi-parallel streamlines form across the ductal segment, a
 176 feature previously seen with *in vitro* models of terminal sacs [18].

177 Instantaneous particle positions are shown in Fig. 4 at three characteristic time points: end
 178 of first inhalation (a,d,g), end of second inhalation (b,e,h) and at the end of the second breath
 179 (c,f,i), where the color-coding indicates airborne (red) or deposited (blue) particles. The majority
 180 of particles remain airborne after the first inhalation ($t = 0.5\tau$, Fig. 4a,d and g) and do not penetrate
 181 as far in the emphysematous regions compared to the normal ones. In particular, particles in the H
 182 model (Fig. 4a) are carried with the ductal flow deep into the acinar structure, whereas the lack of
 183 ductal structures in the emphysematous regions (e.g. E_{hom} , Fig. 4g) causes the velocities to slow
 184 as the cross-sectional area increases. Additionally, most particles either deposited or were exhaled
 185 by the end of the second inhalation in the H model, in contrast to the E_{hom} and E_{het} models, where
 186 particles remained airborne in the diseased regions. However, most particles deposit before the
 187 second exhalation ($t = 1.5\tau$, Fig. 4b,h and e). In contrast, the majority of particles either deposit
 188 or have exited the domain at the proximal inlet/outlet of the H and E_{het} models, respectively. At
 189 the end of the second breath (Fig. 4c,f and i), a small fraction of particles remain airborne in the
 190 emphysematous regions. Videos illustrating the dynamic behavior of inhaled particles are provided
 191 for each model (see SM).

192 Quantitatively, total deposition is larger in the H model (49%) compared to the diseased models
 193 (E_{het} : 38%, E_{hom} : 18%), see Fig. 5. While the majority of deposition occurs during the first
 194 breath, aerosols continue to deposit throughout the respiration cycles (Fig. 5a). The rate of particle

195 deposition is highest at the start of exhalation (Fig. 5), when flow rates are highest (Fig. 2b). We
 196 note that the deposition fraction in the H model plateaus throughout the second breathing cycle,
 197 whereas E_{het} and E_{hom} exhibit a small incline, due to a decreased deposition rate in the emphy-
 198 sematous regions. In an attempt to capture physiologically-relevant deposition metrics, regional
 199 deposition data are extracted and distinguished according to (i) alveolar (i.e. deposition in healthy
 200 alveolar cavities), (ii) ductal (i.e. deposition on the alveolar ring openings and the connecting el-
 201 ements between the generations), and (iii) diseased regions (i.e. deposition in regions where the
 202 ductal and alveolar structures are degenerated). Here, we find that the majority of particles deposit
 203 in the ductal regions of the H and E_{het} models (Fig. 5b); only 14% of the particles deposit inside the
 204 alveolar cavities of the H model. The majority of deposition is seen in the normal regions (normal:
 205 87%, diseased: 13%) for the E_{het} model. As the diseased regions of the E_{hom} and E_{het} models do
 206 not contain septa or distinct alveolar cavities (Fig. 1c, inset), deposition could not be discriminated
 207 between ductal and alveolar regions. Accordingly, particles that deposit in the diseased regions of
 208 the E_{het} and E_{hom} models are labeled as such (Fig. 5, b).

209 Additionally, we assessed final particle deposition penetration depths according to centerline
 210 distances (qualitatively shown in Fig. 4, right column). Here, the centerline starts at the entrance
 211 of the acinar model, follows the duct and ends at the particle deposition site (Fig. 6). It should be
 212 underlined that the penetration depth measured is not equivalent to the particle pathline. Particles
 213 penetrated the deepest in the H model with a mean of $l_H = 0.23$ mm compared to the emphysema-
 214 tous ones with $l_{E_{het}} = 0.2$ mm and $l_{E_{hom}} = 0.16$ mm, respectively. We statistically compared these
 215 mean values using a non-parametric Wilcoxon signed rank test with Bonferroni correction (R pro-
 216 gramming language, Version 3.2.0). Cross-testing all models, we find that means are significantly
 217 different between all models ($p \ll 0.001$). Qualitatively, particle deposition fractions are similar
 218 between the H and E_{het} models for particles that deposited within 0.2 mm of the entrance. More
 219 particles deposited in the H model compared to the E_{het} model for penetration depths > 0.2 mm.

220 The drop in particle deposition in the distal generations of the E_{het} region is correlated with the
221 entrance to the diseased region (0.24 mm from the entrance). Indeed, deposition mainly occurs
222 at the entrance and first generations of the E_{hom} model while distal regions are nearly depleted of
223 particles (Figs. 4 and 6).

224 Finally, we assessed particle concentrations by superimposing a 3D voxel grid and counting
225 the number of deposited particles per voxel (Fig. 7). Here, the sensitivity of concentration with
226 respect to the voxel size was first tested (i.e. the larger the voxel size the more particles contained
227 within the voxel); as the trends were independent of voxel size, a final voxel size of 10 μm lateral
228 length (approximately 1/3 of the alveolar diameter) was eventually chosen. Generally, particle
229 concentration was highest at the entrance of H (Fig. 7a) and E_{het} models (Fig. 7b). Furthermore,
230 concentration is relatively uniform in the H model as the particles reached all generations of the
231 model. In contrast, fewer particles reached, and thus deposited in the diseased regions of the E_{het}
232 and E_{hom} models. Motivated by the deposition data collected in rats [17], the relative dispersion
233 (RD) was calculated by dividing the standard deviation of all voxel concentrations by their average.
234 A clear trend is noted where RD increases with increasing emphysematous region, such that E_{hom}
235 yields the largest RD (Fig. 7d). This finding further underlines localized deposition phenomena in
236 emphysematous regions in E_{het} and E_{hom} , as noted in Fig. 7b,c and previously in Fig. 6.

237 Discussion

238 Despite the high prevalence of emphysema, there are few studies aimed at understanding dif-
239 ferences in particle deposition between healthy and emphysematous lungs [3, 17, 26]. Due to ex-
240 perimental feasibility, these studies only report global deposition, thus rendering it unclear which
241 mechanisms are the underlying causes of deposition differences in emphysema. While it has been
242 previously shown that an increase in tissue compliance results in enhanced delivery of airborne par-
243 ticles to the diseased lung regions [19], the fate of particles once they reach the alveolated airways
244 remains largely unknown. Motivated by recent experimental [17] and numerical studies [19, 20]

in rat lungs, we performed particle-laden airflow simulations in multi-generational acinar models (Fig. 1). One healthy and two distinct emphysema models were designed in an effort to assess disease severity, where diseased regions were distributed either heterogeneously (E_{het} , Fig. 1c) or homogeneously (E_{hom} , Fig. 1d). Emphysematous regions were created by removing the septa between alveolar cavities and enlarging the alveolar volume. As such, the emphysematous models represent panacinar emphysema [29, 30], a type of emphysema associated with alpha1-antitrypsin deficiency found in elderly patients [29]. Panacinar emphysema is analogous to the one elastase creates in rat lungs [2, 16].

Our findings indicate that micron-sized particles deposit mainly during the first breathing cycle and the deposition rate is maximum at the start of the first exhalation (Fig. 5a). Compared to the E_{hom} and E_{het} models, deposition is enhanced in the healthy (H) model (Fig. 5) due to the presence of inter-septal walls and alveolar rings (Fig. 1) and the larger normalized tidal volume in the H model (Fig. 2) compared to the emphysematous models. Absolute tidal volumes of all models were kept the same to match the experimental ventilation settings [17], such that deposition differences between the models are anticipated to result from geometric differences and ensuing flow characteristics. Namely, inter-septal walls under healthy conditions create flow boundaries between the alveolar cavities and the acinar ducts [6, 9, 28], resulting in relatively fast ductal flows compared to slow, recirculating flows in the alveolar cavities (Fig. 3, proximal insert). Consequently, the particle-laden air is carried deeper into the acinus of the H model, resulting in enhanced penetration depths in health compared to emphysema (see Fig. 4 and SM), as was previously shown in an *in vitro* alveolar sac [18] and acinar model [1]. This resulted in fewer particles depositing in the distal areas of the models (Fig. 4 and Fig. 6).

Total deposition was found to be higher in the E_{het} model compared to the E_{hom} model with the majority of particles depositing in the normal regions (Fig 5), despite nearly the same regional FRC (Table 1). Comparing the H and E_{het} model, slightly more particles deposited on the healthy

270 airways leading to the diseased region of the E_{het} model caused by larger tidal volume of the
 271 distal diseased segments and accordingly, resulted in more particle-laden air to travel through these
 272 airways. Particle deposition was higher in the outer sleeve (i.e. the former alveolar cavities) of
 273 the emphysematous models compared to the alveolar cavities in the H model, as the E_{hom} and E_{het}
 274 models hold no inter-septal walls. Particles that entered the emphysematous regions were more
 275 likely to remain suspended after the first breath (Fig. 4) and travelled slightly deeper during the
 276 subsequent breath in the diseased zones (see Fig. 4 and SM). This is a result of a net gravitational
 277 sedimentation with a deviation from the original pathline such that particles are not exhaled. While
 278 airborne particles may deposit upon subsequent breaths, only $\sim 1.2\%$ of inspired particles remained
 279 suspended representing a minor role on total deposition. Particles may become trapped if the
 280 small airways collapse upon exhalation, a phenomenon not captured here, but known to occur in
 281 emphysema [12]. This will likely result in enhanced particle deposition in these regions given
 282 that particles will have more time to migrate to the airway walls. Such an effect could explain
 283 the disparities between model predictions and the experimental work by Oakes et al. [17], where
 284 higher deposition was measured in disease.

285 While direct comparison of model predictions with *in vivo* experimental data is not currently
 286 feasible, as a single voxel of the experimental MRI data contains a combination of small airways
 287 and acinar structures, some general comparisons may be made. First, in contrast to the rat experi-
 288 ments [17], we predicted less deposition in emphysema; this latter trend is however in agreement
 289 with an *in vivo* study performed in hamsters [26], an *in vitro* model [18] and a stochastic model [23].
 290 Here, the relative dispersion (RD) represents a measure of the uniformity of the deposited particle
 291 concentration, where a larger RD thus indicates a more heterogeneous distribution of deposited
 292 particles. In agreement with the experimental data of Oakes et al. [17], we showed that RD was
 293 larger in the emphysematous models compared to the H models (Fig. 7d). Namely, the E_{hom} model
 294 had the largest RD compared to the other two models (Fig. 7d), underlining regions of high particle

295 concentration (hot spots) and areas where particles did not deposit (Fig. 7c).

296 In a recent numerical study in the rat conducting airways, Oakes et al. [19] predicted that,
297 due to the enhanced respiratory compliance, more particle-laden air would reach the respiratory
298 zone of the diseased regions of a heterogenous emphysematous lung compared to normal regions.
299 However, the fate of the particles once they enter the respiratory zone, and thus the influence
300 of the morphometric changes that occur in emphysema was not investigated. This resulted in a
301 non-favourable comparison between the numerical predictions and the experimental data for the
302 emphysematous rats. Indeed, Oakes et al. [17] showed that particle deposition was higher in the
303 healthy lobes of the emphysematous rat compared to the diseased lobes. Motivated by the inability
304 of the previous numerical study [19] to uncover the mechanisms behind the deposition differences
305 between the healthy and emphysematous rats, we have shown that in the absence of alveolar rings
306 in the diseased regions of the E_{het} model (Fig. 1), more particles deposit in the normal regions of the
307 E_{het} model compared to the diseased regions. Hence, a heterogeneous distribution of emphysema
308 leads to higher deposition efficiency in the normal regions of the lung compared to the diseased
309 ones; this latter finding may help explain the enhanced deposition found experimentally in the
310 normal regions of the rat [17].

311 Characterizing an inherently heterogeneous disease such as emphysema is challenging and
312 entails a set of reasonable assumptions and limitations. The numerical limitations of the utilized
313 solver, boundary conditions and computational mesh were recently discussed [10]. Instead, we
314 focus on discussing limitations pertaining to modelling emphysema. To transform the human sub-
315 acinar model [10] to dimensions representative of a rat, a uniform scaling was assumed between rats
316 and humans, and thus the smaller ratio of duct length to duct diameter ratio in rats [21] compared
317 to humans [33] was not accounted for. However, as the goal of this study was to compare the
318 influence of homogeneously and heterogeneously distributed emphysema on particle deposition,
319 we anticipate that this choice of scaling will have little influence on the results. As mentioned,

320 airway collapse is common during emphysema, a feature not mimicked in the present acinar model.
321 Airway collapse may raise deposition fractions in the diseased regions. While deterioration of
322 alveolar septa and enhanced alveolar volume are characteristic of emphysema, our model does not
323 capture all changes that occur with emphysema. For example, alveoli may increase in size and
324 change in shape [29], potentially further decreasing deposition in disease. Due to computational
325 costs, it is currently infeasible to model the entire lung for all spatial and temporal dimensions, thus
326 direct comparison between model predictions and experimental data cannot be made. The present
327 work would certainly benefit from ventilation distribution maps [4, 12] or further experimental data
328 in deposition in the lungs [32]. While this study addresses rat lungs, changes in flow structures in
329 human lungs between the normal and diseased regions are likely to bear resemblance, where similar
330 results could be anticipated.

331 By simulating particle transport in healthy and emphysematous acini, we were able to uncover
332 the potential influence of emphysema-like geometric changes on acinar deposition. By implement-
333 ing similar flow curves and particle properties of recent experiments in rat lungs [17, 20], com-
334 parison between our numerical predictions and experimental data were made. Our main findings
335 are decreased deposition in the emphysematous models compared to the healthy model as well as
336 increased dispersion in the diseased acini. Particle deposition in emphysematous acini is biased to-
337 wards proximal acinar generations, while relative dispersion of particle concentrations is increased.
338 As these findings are not entirely in agreement with previous studies (e.g. Oakes et al. [17]), other
339 mechanisms are anticipated to influence deposition outcomes between the healthy and emphyse-
340 matous rats. Hence, physiological factors such as small airway collapse, particle trapping and/or
341 whole-lung heterogeneity, are hypothesized to be responsible for the enhanced deposition found
342 experimentally.

343 Acknowledgements

344 J. M. Oakes was supported by a Whitaker International Scholarship administrated by the Inter-
345 national Institute of Education, an INRIA Associated Team Postdoctoral Grant and an University
346 of California Presidential Postdoctoral Fellowship. P. Hofemeier and J. Sznitman were supported
347 by the Israel Science Foundation (Grant nr. 990/12).

348 Conflict of interest

349 The authors have no conflict of interest related to the work presented in this manuscript.

350 Supplementary Information

351 **SM1:** 3D visualization of the H (SM1a.avi), E_{het} (SM1b.avi) and E_{hom} model (SM1c.avi),
352 where light grey indicates healthy and dark grey diseased regions. Rotation of the domain is first
353 shown to illustrate the bifurcating acinar tree structure; next, a representative breathing cycle is
354 shown highlighting the expansion and contraction of the domain. Note the asynchronous breathing
355 pattern of the healthy and diseased zone in SM1b.

356 **SM2:** Particle positions over two complete breathing cycles for the H (SM2a.avi), E_{het} (SM2b.avi)
357 and E_{hom} model (SM2c.avi): Color-coding indicates airborne (red) and deposited (blue) particles.

358 References

- 359 [1] Berg, E.J., Robinson, R.J., 2011. Stereoscopic particle image velocimetry analysis of healthy
360 and emphysemic alveolar sac models. *Journal of Biomechanical Engineering* 133, 061004.
361 URL: <http://www.ncbi.nlm.nih.gov/pubmed/21744924>, doi:10.1115/1.4004251.
- 362 [2] Borzone, G., Liberona, L., Olmos, P., Sáez, C., Meneses, M., Reyes, T., Moreno, R., Lisboa,
363 C., 2007. Rat and hamster species differences in susceptibility to elastase-induced pulmonary
364 emphysema relate to differences in elastase inhibitory capacity. *American Journal of Physi-*
365 *ology. Regulatory, Integrative and Comparative Physiology* 293, R1342–9.

- 366 [3] Brand, P., Schulte, M., Wencker, M., Herpich, C.H., Klein, G., Hanna, K., Meyer, T.,
367 2009. Lung deposition of inhaled alpha1-proteinase inhibitor in cystic fibrosis and alpha1-
368 antitrypsin deficiency. *The European Respiratory Journal* 34, 354–60.
- 369 [4] Emami, K., Chia, E., Kadlecsek, S., Macduffie-Woodburn, J.P., Zhu, J., Pickup, S., Blum, A.,
370 Ishii, M., Rizi, R.R., 2011. Regional correlation of emphysematous changes in lung function
371 and structure: a comparison between pulmonary function testing and hyperpolarized MRI
372 metrics. *Journal of Applied Physiology* 110, 225–235.
- 373 [5] Fishler, R., Hofemeier, P., Etzion, Y., Dubowski, Y., Sznitman, J., 2015. Particle dynamics
374 and deposition in true-scale pulmonary acinar models. *Scientific Reports* .
- 375 [6] Fishler, R., Mulligan, M.K., Sznitman, J., 2013. Acinus-on-a-chip: A microfluidic platform
376 for pulmonary acinar flows. *Journal of Biomechanics* 46, 2817–2823.
- 377 [7] Fung, Y.C., 1988. A model of the lung structure and its validation. *Journal of Applied*
378 *Physiology* 64, 2132–2141.
- 379 [8] Harding, E.M., Robinson, R.J., 2010. Flow in a terminal alveolar sac model with expanding
380 walls using computational fluid dynamics. *Inhalation Toxicology* 22, 669–78.
- 381 [9] Hofemeier, P., Sznitman, J., 2014. Role of alveolar topology on acinar flows and convective
382 mixing. *Journal of Biomechanical Engineering* 136, 061007.
- 383 [10] Hofemeier, P., Sznitman, J., 2015. Revisiting acinar particle transport: convection, sedimen-
384 tation, diffusion and their interplay. *Journal of Applied Physiology* 118, 1375–1385.
- 385 [11] Hogg, J.C., 2004. Pathophysiology of airflow limitation in chronic obstructive pulmonary
386 disease. *Lancet* 364, 709–721.

- 387 [12] Jacob, R.E., Carson, J.P., Thomas, M., Einstein, D.R., 2013. Dynamic multiscale boundary
388 conditions for 4D CT of healthy and emphysematous rats. *PloS One* 8, e65874.
- 389 [13] Khajeh-Hosseini-Dalasm, N., Longest, P.W., 2015. Deposition of particles in the alveolar
390 airways: Inhalation and breath-hold with pharmaceutical aerosols. *Journal of Aerosol Science*
391 79, 15–30.
- 392 [14] Kumar, H., Tawhai, M.H., Hoffman, E.a., Lin, C.L., 2009. The effects of geometry on airflow
393 in the acinar region of the human lung. *Journal of Biomechanics* 42, 1635–42.
- 394 [15] Ma, B., Darquenne, C., 2011. Aerosol deposition characteristics in distal acinar airways under
395 cyclic breathing conditions. *Journal of Applied Physiology* 110, 1271–1282.
- 396 [16] March, T.H., Green, F.H.Y., Hahn, F.F., Nikula, K.J., 2000. Animal models of emphysema
397 and their relevance to studies of particle induced disease. *Inhalation Toxicology* 12, 155–187.
- 398 [17] Oakes, J.M., Breen, E., Scadeng, M., Tchantchou, G.S., Darquenne, C., 2014a. MRI-based
399 measurements of aerosol deposition in the lung of healthy and elastase-treated rats. *Journal*
400 *of Applied Physiology* 116, 1561–1568.
- 401 [18] Oakes, J.M., Day, S., Weinstein, S.J., Robinson, R.J., 2010. Flow field analysis in expanding
402 healthy and emphysematous alveolar models using particle image velocimetry. *Journal of*
403 *Biomechanical Engineering* 132, 021008–1–9.
- 404 [19] Oakes, J.M., Marsden, A.L., Grandmont, C., Darquenne, C., Vignon-Clementel, I.E., 2015.
405 Distribution of aerosolized particles in healthy and emphysematous rat lungs: Comparison
406 between experimental and numerical studies. *Journal of Biomechanics* 48, 1147–1157.
- 407 [20] Oakes, J.M., Marsden, A.L., Grandmont, C., Shadden, S.C., Darquenne, C., Vignon-
408 Clementel, I.E., 2014b. Airflow and particle deposition simulations in health and emphysema:
409 from in vivo to in silico animal experiments. *Annals of Biomedical Engineering* 42, 899–914.

- 410 [21] Rodriguez, M., Bur, S., Favre, A., Weibel, E.R., 1987. Pulmonary acinus: geometry and
411 morphometry of the peripheral airway system in rat and rabbit. *The American Journal of*
412 *Anatomy* 180, 143–55.
- 413 [22] Rubio, M.L., Sánchez-Cifuentes, M.V., Peces-Barba, G., Verbanck, S., Paiva, M., González
414 Mangado, N., 1998. Intrapulmonary gas mixing in panacinar- and centriacinar-induced em-
415 physema in rats. *American Journal of Respiratory and Critical Care Medicine* 157, 237–45.
- 416 [23] Sturm, R., Hofmann, W., 2004. Stochastic simulation of alveolar particle deposition in lungs
417 affected by different types of emphysema. *Journal of Aerosol Medicine* 17, 357–72.
- 418 [24] Suki, B., Lutchen, K.R., Ingenito, E.P., 2003. On the progressive nature of emphysema:
419 Roles of proteases, inflammation, and mechanical forces. *American Journal of Respiratory*
420 *and Critical Care Medicine* 168, 516–521.
- 421 [25] Suki, B., Parameswaran, H., 2014. Computational modeling helps uncover mechanisms re-
422 lated to the progression of emphysema. *Drug Discovery Today: Disease Models* 70, 4245–
423 4249.
- 424 [26] Sweeney, T.D., Brain, J.D., Leavitt, S.a., Godleski, J.J., 1987. Emphysema alters the de-
425 position pattern of inhaled particles in hamsters. *The American Journal of Pathology* 128,
426 19–28.
- 427 [27] Sznitman, J., 2009. Convective gas transport in the pulmonary acinus: Comparing roles of
428 convective and diffusive lengths. *Journal of Biomechanics* 42, 789–792.
- 429 [28] Sznitman, J., 2013. Respiratory microflows in the pulmonary acinus. *Journal of Biomechanics*
430 46, 284–98.
- 431 [29] Takahashi, M., Fukuoka, J., Nitta, N., Takazakura, R., Nagatani, Y., Murakami, Y., Otani,

- 432 H., Murata, K., 2008. Imaging of pulmonary emphysema: a pictorial review. International
433 Journal of Chronic Obstructive Pulmonary Disease 3, 193–204.
- 434 [30] Thurlbeck, W.M., Muller, N.L., 1994. Emphysema: Definition, Imaging, and Quantification.
435 American Journal of Roentgenology 163, 1017–1025.
- 436 [31] Ueno, M., Maeno, T., Nishimura, S., Ogata, F., Masubuchi, H., Hara, K., Yamaguchi, K.,
437 Aoki, F., Suga, T., Nagai, R., Kurabayashi, M., 2015. Alendronate inhalation amelio-
438 rates elastase-induced pulmonary emphysema in mice by induction of apoptosis of alveolar
439 macrophages. Nature Communications 6, 6332–6345.
- 440 [32] Wang, H., Sebr  , C., Ruaud, J.P., Guillot, G., Bouazizi-Verdier, K., Willoquet, G., Ma  tre,
441 X., Darrasse, L., de Rochefort, L., 2015. Aerosol deposition in the lungs of spontaneously
442 breathing rats using Gd-DOTA-based contrast agents and ultra-short echo time MRI at 1.5
443 Tesla. Magnetic Resonance in Medicine In Press.
- 444 [33] Weibel, E., 1965. Morphometry of the human lung, Springer.

445 List of Figures

446	1	Schematic of the multi-generational acinar models of the 3D computational domain	
447		for the: (a) healthy, H , (c) heterogeneous emphysematous, E_{Het} , and (d) homoge-	
448		neous emphysematous E_{Hom} cases. Light grey and dark grey denote the normal	
449		and diseased regions, respectively. A diagram of the acinar tree is shown in (b)	
450		where the diseased region of the E_{Het} model is highlighted in grey. Inset in (c)	
451		depicts the alveolar structure where inter-septal walls are outlined in purple (light	
452		grey region). No inter-septal walls are present in the diseased regions (dark grey	
453		region).	23
454	2	Inspired volume curves, $V_A(t)$, normalized by the FRC_A of the three models (top	
455		panel), and corresponding flow rates (bottom panel) for the three simulation cases.	
456		Volume (normalized by FRC_A of the whole model) and corresponding flow curves	
457		for the diseased and normal zones are shown separately for the E_{het} case.	24
458	3	Instantaneous 2D projections of representative 3D flow streamlines is shown at	
459		peak inspiration ($t = \tau/8$) for the E_{het} model. Streamlines are color-coded (loga-	
460		rithmic scale) according to the local velocity magnitudes normalized by the maxi-	
461		mal velocity at the inlet of the model. Four regions of the model are highlighted in	
462		the respective insets: proximal, medial, distal and diseased.	25
463	4	Snapshots of particle locations in the three acinar models captured at three time	
464		points during the breathing cycle. Particles in red are airborne (i.e. not deposited)	
465		and particles in blue are deposited. Corresponding movies of particle motions for	
466		the different cases are provided in the supplementary material (SM).	26
467	5	(a) Deposition fraction as a function of cumulative breathing cycles. Particles were	
468		injected throughout the inspiration phase of the first breath, from $t = 0\tau$ to $t = 0.5\tau$.	
469		(b) Final deposition fraction partitioned according to alveolar and ductal regions;	
470		the corresponding deposition fraction in the region of the emphysematous models	
471		is shown. Note that for such cases, the diseased regions cannot be distinguished	
472		according to alveolar and ductal regions in the absence of alveolar walls.	27

473	6	Deposition fraction plotted as a function of the penetration depth measured from	
474		the acinar entrance for the three acinar models, respectively. Penetration depths	
475		were taken after the second breath for deposited particles only, thus remaining	
476		airborne particles were not included in the calculation. Note that the penetration	
477		depths only assess the distance to the inlet of the domain, by calculating a particle's	
478		distance to the centreline of the duct and subsequently the distance (following the	
479		centreline of the duct) to the inlet.	28
480	7	Deposited particle concentrations for the: (a) H , (b) E_{het} and (c) E_{hom} acinar mod-	
481		els, respectively. Here, concentration is defined as the number of particles de-	
482		posited within a voxel size with length of $10\ \mu\text{m}$. Panel (d) shows the relative	
483		dispersion (RD), defined as the standard deviation normalized by the mean of the	
484		particle concentration for each acinar model [17]. Note that areas where particles	
485		did not deposit on were included in the RD calculation.	29

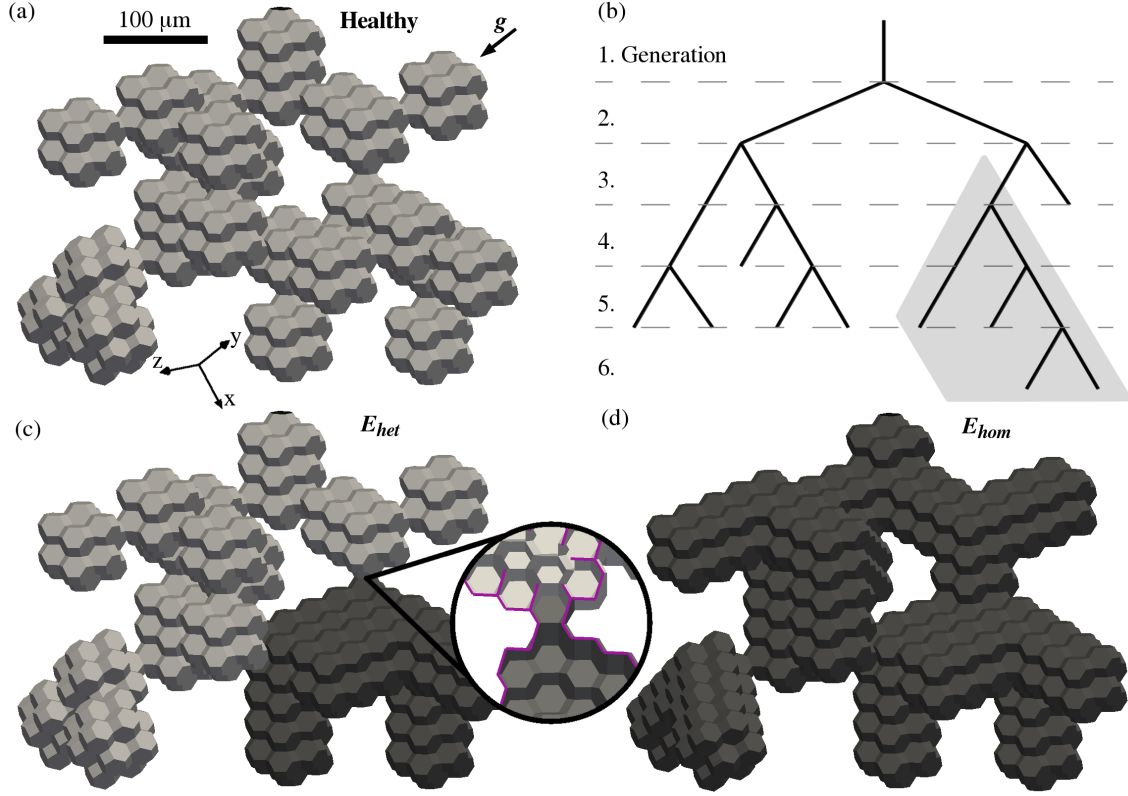


Figure 1: Schematic of the multi-generational acinar models of the 3D computational domain for the: (a) healthy, H , (c) heterogeneous emphysematous, E_{het} , and (d) homogeneous emphysematous E_{hom} cases. Light grey and dark grey denote the normal and diseased regions, respectively. A diagram of the acinar tree is shown in (b) where the diseased region of the E_{het} model is highlighted in grey. Inset in (c) depicts the alveolar structure where inter-septal walls are outlined in purple (light grey region). No inter-septal walls are present in the diseased regions (dark grey region).

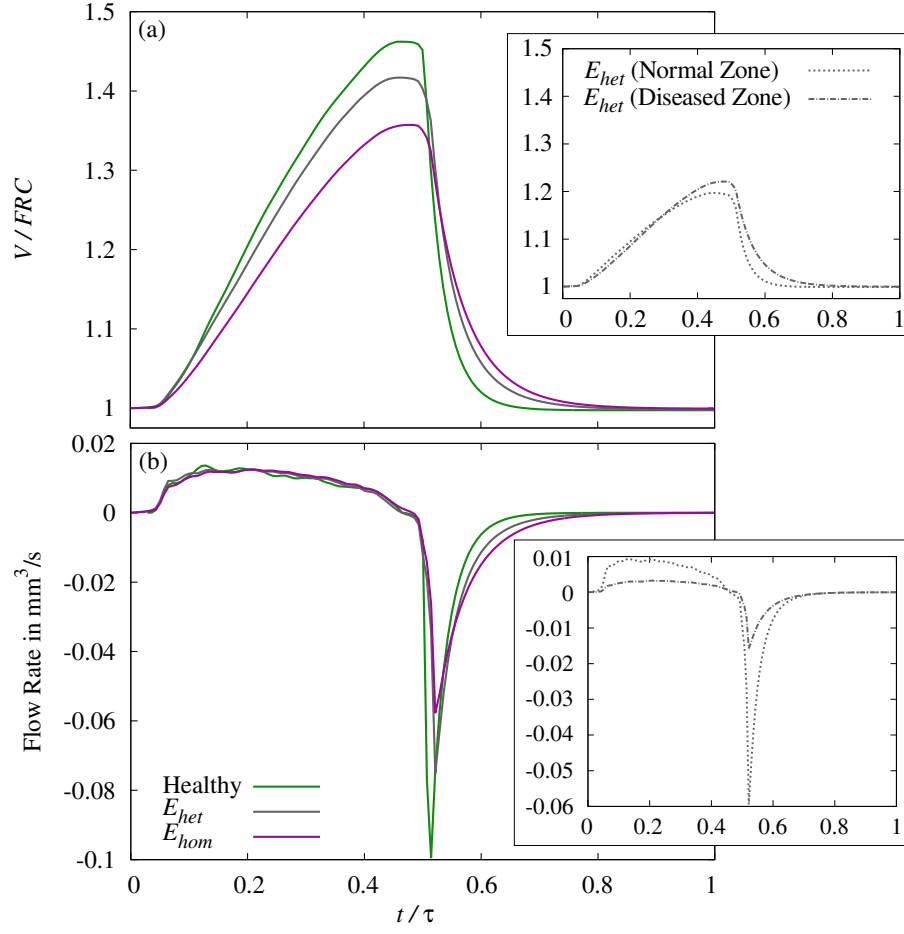


Figure 2: Inspired volume curves, $V_A(t)$, normalized by the FRC_A of the three models (top panel), and corresponding flow rates (bottom panel) for the three simulation cases. Volume (normalized by FRC_A of the whole model) and corresponding flow curves for the diseased and normal zones are shown separately for the E_{het} case.

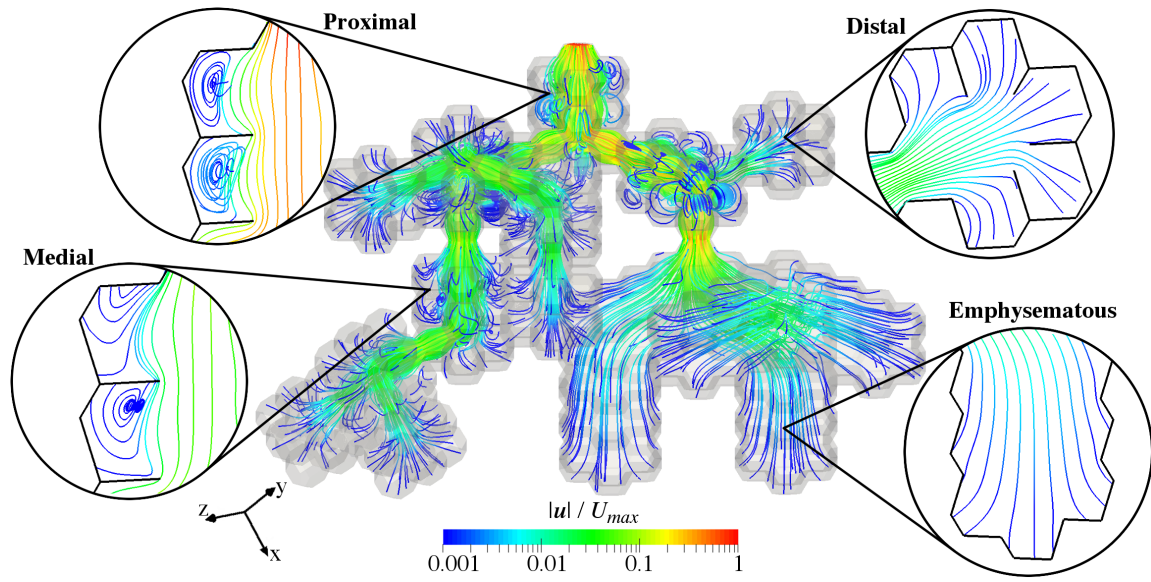


Figure 3: Instantaneous 2D projections of representative 3D flow streamlines is shown at peak inspiration ($t = \tau/8$) for the E_{het} model. Streamlines are color-coded (logarithmic scale) according to the local velocity magnitudes normalized by the maximal velocity at the inlet of the model. Four regions of the model are highlighted in the respective insets: proximal, medial, distal and diseased.

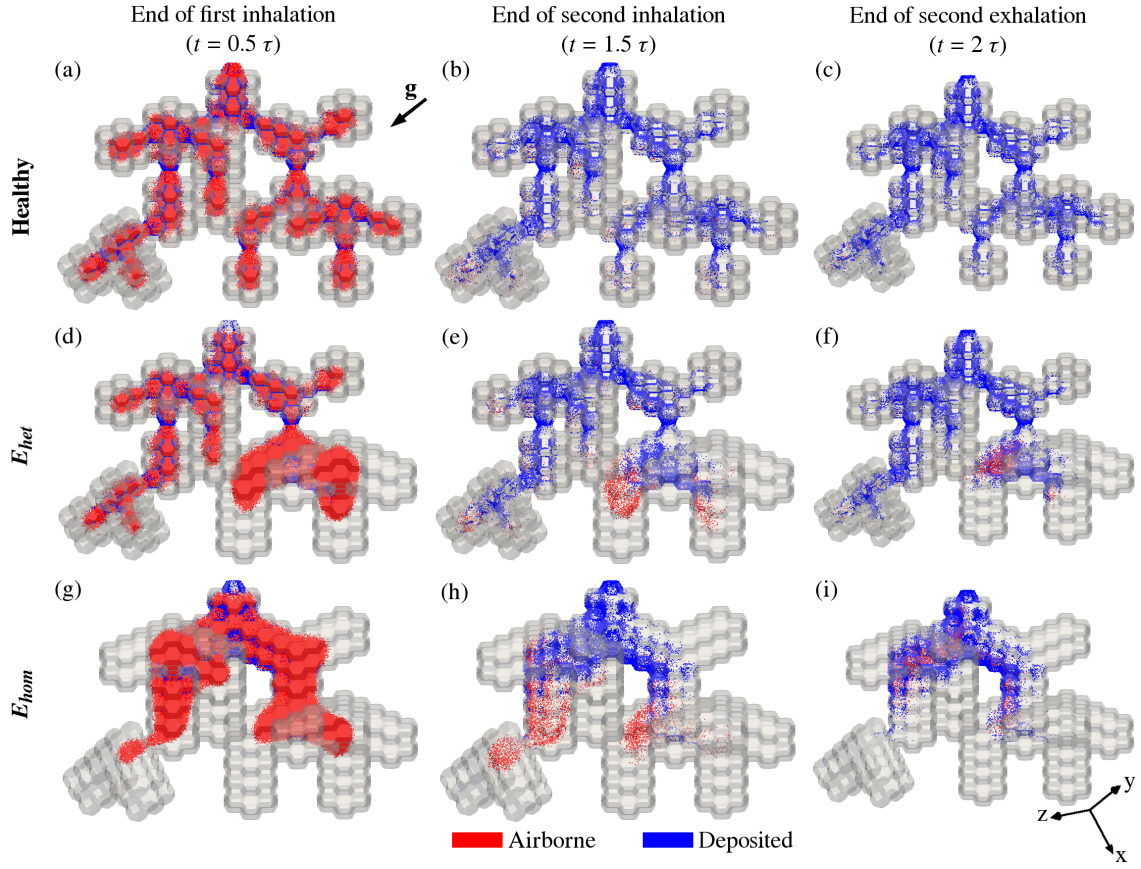


Figure 4: Snapshots of particle locations in the three acinar models captured at three time points during the breathing cycle. Particles in red are airborne (i.e. not deposited) and particles in blue are deposited. Corresponding movies of particle motions for the different cases are provided in the supplementary material (SM).

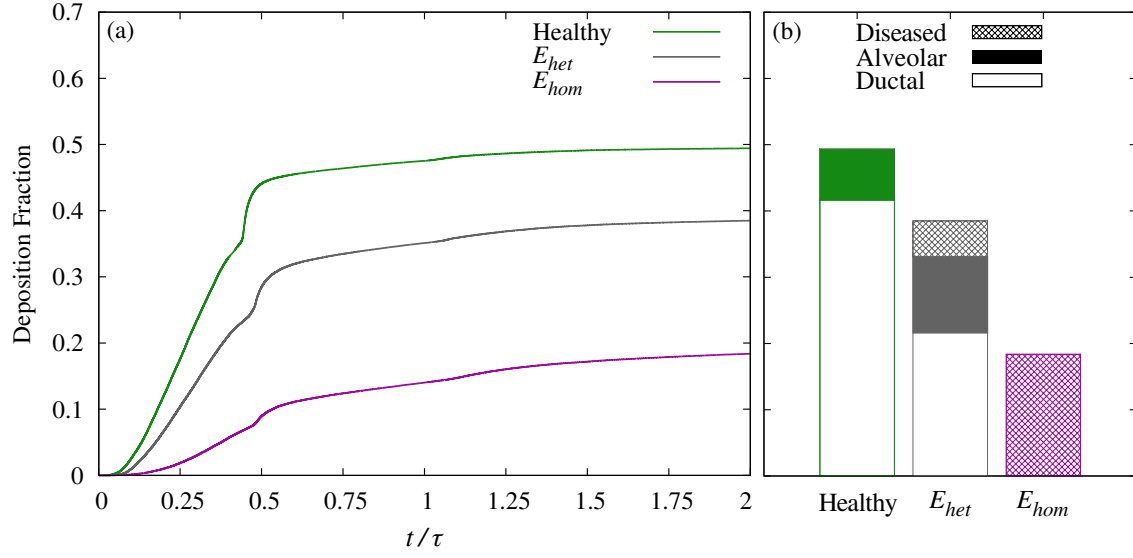


Figure 5: (a) Deposition fraction as a function of cumulative breathing cycles. Particles were injected throughout the inspiration phase of the first breath, from $t = 0\tau$ to $t = 0.5\tau$. (b) Final deposition fraction partitioned according to alveolar and ductal regions; the corresponding deposition fraction in the region of the emphysematous models is shown. Note that for such cases, the diseased regions cannot be distinguished according to alveolar and ductal regions in the absence of alveolar walls.

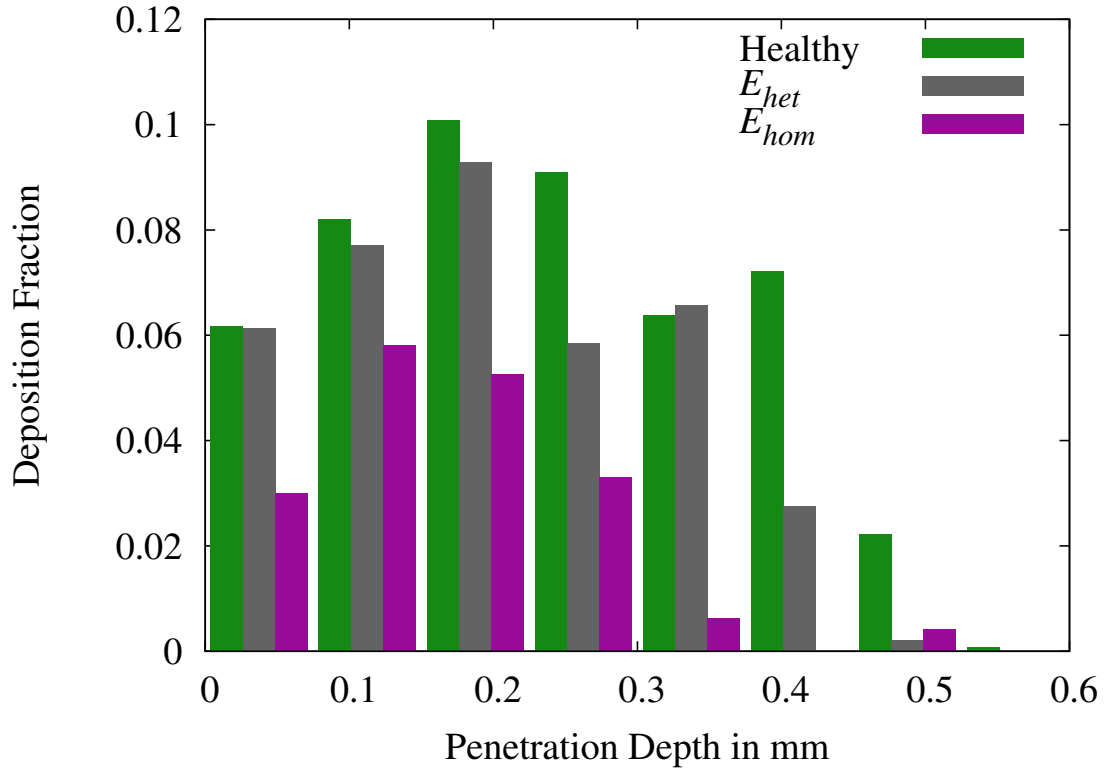


Figure 6: Deposition fraction plotted as a function of the penetration depth measured from the acinar entrance for the three acinar models, respectively. Penetration depths were taken after the second breath for deposited particles only, thus remaining airborne particles were not included in the calculation. Note that the penetration depths only assess the distance to the inlet of the domain, by calculating a particle's distance to the centreline of the duct and subsequently the distance (following the centreline of the duct) to the inlet.

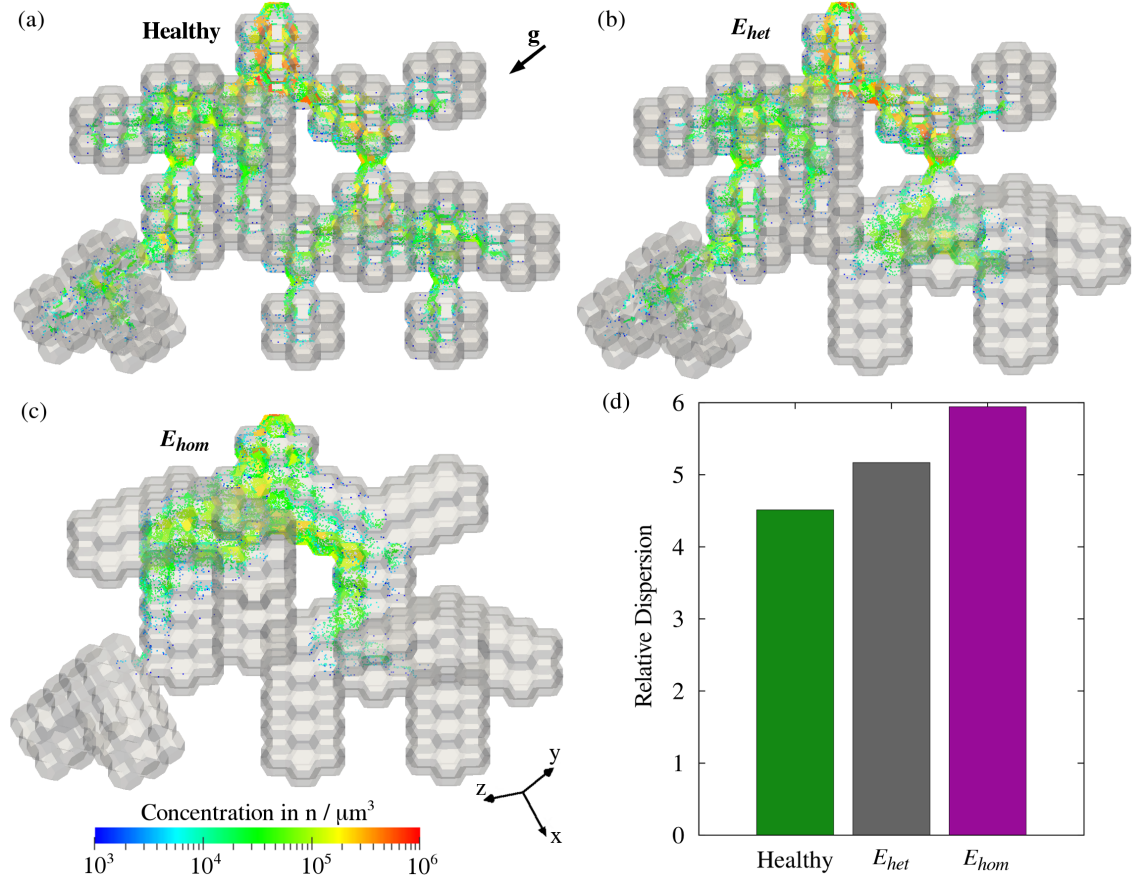


Figure 7: Deposited particle concentrations for the: (a) H , (b) E_{het} and (c) E_{hom} acinar models, respectively. Here, concentration is defined as the number of particles deposited within a voxel size with length of $10 \mu\text{m}$. Panel (d) shows the relative dispersion (RD), defined as the standard deviation normalized by the mean of the particle concentration for each acinar model [17]. Note that areas where particles did not deposit on were included in the RD calculation.

486 **List of Tables**

487	1	Morphological properties of the healthy (H), heterogeneous emphysematous (E_{Het})	
488		and homogeneous emphysematous (E_{Hom}) model at functional residual capacity	
489		(FRC).	31

Table 1: Morphological properties of the healthy (H), heterogeneous emphysematous (E_{Het}) and homogeneous emphysematous (E_{Hom}) model at functional residual capacity (FRC).

Model	Alveolar cavities	Volume $10^{-3}mm^3$	S/V mm^{-1}	Tidal Volume $10^{-3}mm^3$
Healthy, H	277	5.9	163.7	2.72
Homogeneous Emphysema, E_{hom}	0	7.8	72.2	2.72
Heterogeneous Emphysema, E_{het}	180	6.6	125.6	2.72
E_{het} : Normal Zone	180	3.8	109.1	1.30
E_{het} : Diseased Zone	0	2.8	73.9	1.42